Supplementary Information for

Edge-driven collapse of fluid holes

Huanlei Zhao,[1] Bin Zhang,[1] Cunjing Lv[1,2*]

[1]Department of Engineering Mechanics, AML, Tsinghua University, 100084 Beijing, China

[2]Center for Nano and Micro Mechanics, Tsinghua University, 100084 Beijing, China

Content

* To whom correspondence should be addressed. Email: cunjinglv@tsinghua.edu.cn

S1. Surface Evolver (SE) simulations

S1.1. Introduction of the simulations by employing SE

As shown in the left panel of figure 6(*a*) from different views, the configuration of the film is initialized in a polyhedral shape. Subsequently, the surface is evolved in a loop of iterations and mesh refinement operations until a convergence criterion is met. Then the initial configuration transitions to the final stable configuration is shown in the right panels of figure 6(*a*). The details of our initial configuration are shown in figure S1, where the diameter d and thickness h are indicated. The final stable configuration is in the minimum energy position, and post-processing is employed to obtain the volume of liquid Ω and the area of the hole A. Water is added artificially into the liquid layer by increasing the volume in SE program. Therefore, a series of stable liquid layer configurations with volume smaller than the critical volume Ω_c can be simulated in SE program. The results are presented in figure 6(*b*), in which the container diameter is d = 9 cm, the contact angle of substrate is θ_s = 160°, and the contact angle of wall is θ_w = 90°.

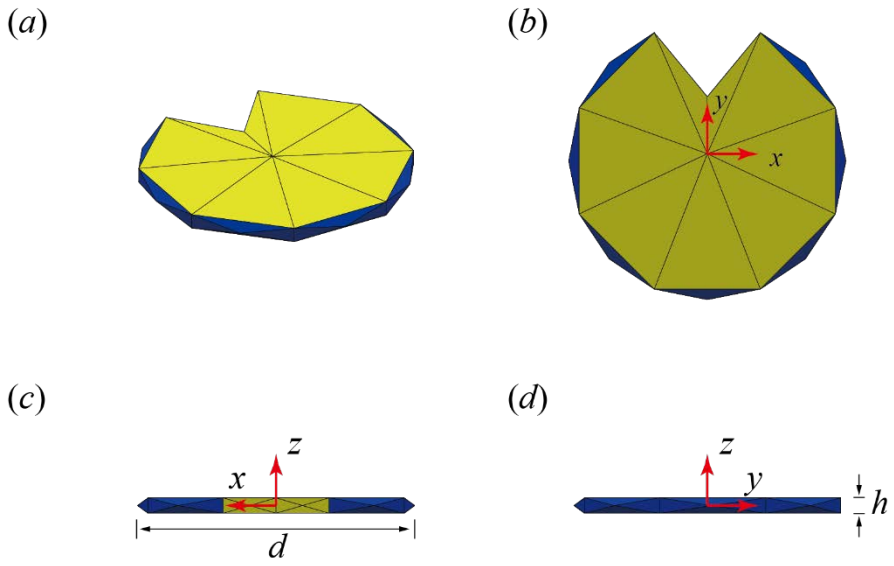

Fig. S1. Initial configuration of a liquid layer with a near-wall hole. For better visualization, different colors are used to denote the facets of different regions: the yellow color represents the liquid-vapor surface while the blue color represents the liquid-solid surface. (*a*) The initial configuration from an oblique view. (*b*) The initial configuration from a top view. (*c*) The initial configuration from a front view. (*d*) The initial configuration from a side view. The diameter d and thickness h of the liquid layer are indicated.

S1.2. Evolution process of SE

During a simulation, SE takes virtual displacements to reduce the total energy in each iteration. After several thousand iterations, the liquid surface becomes smooth and the energy of the system approaches an asymptotical value, and we denote this value as E_0. In order to find E_0, we define a tolerance interval $\delta_{i-1} = |E_{i-1} - E_i|/\gamma l_c^2$, denoting E_i the energy at ith iteration as shown figure S2. When $\delta_i < 10^{-5}$, we suppose it is close enough to the asymptotic state, i.e., $E_{i-1} \approx E_i \approx E_0$. Typically, in our simulations, convergence is reached after several thousand iterations with 10^4-10^5 triangular facets.

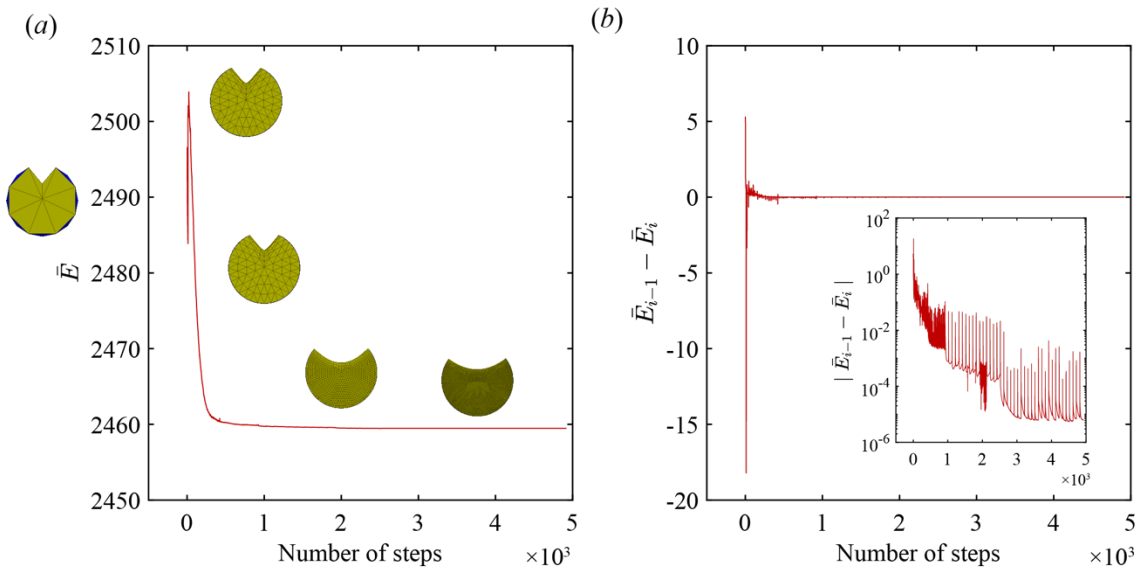

Fig. S2. (*a*) Iteration process of SE. The red line represents the evolution of the dimensionless energy of the system. The insets are the configurations of the liquid film at different stages of the iteration process. (*b*) Evolution of the dimensionless quantities $E_{i-1} - E_i$ and $|E_{i-1} - E_i|$.

S1.3. Limitations of SE

Even though SE is effective in obtaining the configuration of liquid films in wetting modes I and II, it has two limitations that make it incapable of capturing the wetting mode III. First, SE is unable to simulate the dynamic behavior of the water film. In wetting mode III, the front of the water film rapidly spreads along the inner wall as the liquid layer is supplied, eventually causing the left and right fronts of the water film to merge at the wall. Consequently, the hole

at the wall transforms into an inner hole within the water film. However, SE lacks the capability to automatically simulate this dynamic transition. Second, SE does not automatically account for contact line pinning and therefore cannot accurately reflect the real physical behavior. It is important to note that obvious contact line pinning exists at the hydrophilic wall in the experiment, which affects the configuration of the liquid film. However, SE does not consider contact line pinning and can only generate an ideal configuration of a liquid ring when the wall is hydrophilic. As a result, we are not able to capture wetting mode III by employing SE.

S2. Lattice Boltzmann Method (LBM) simulations

S2.1. Introduction of the simulations by employing LBM

Lattice-Boltzmann Method (LBM) is developed based on the lattice gas automata.[1] The fundamental idea of LBM is to solve the discrete lattice Boltzmann equation on the regular lattices. LBM owns a lot of advantages, such as simple arithmetic calculations, more efficient of parallelism and feasible abilities of complex boundaries. In this regard, LBM is successfully applied in simulating the problems of flow in porous materials,[2] particle suspensions,[3] static and dynamic wetting phenomena on smooth and rough surfaces[4,5] and so on.

Here, the wetting behavior of liquid layers with a near-wall hole is simulated by employing a three-dimensional D3Q19 model with Bhatnagar-Gross-Krook approximation which is a simple linearized version of the collision operator that makes use of a single relaxation time towards the local equilibrium[6]. The lattice Boltzmann equation from a discrete kinetic equation for the particle distribution function is

$$f_i\left(\mathbf{r}+\mathbf{e}_i\Delta t, t+\Delta t\right) = f_i\left(\mathbf{r}, t\right) - \frac{\left[f_i\left(\mathbf{r}, t\right) - f_i^{\mathrm{eq}}\left(\mathbf{r}, t\right)\right]}{\tau}, \tag{S1}$$

where f_i is the particle velocity distribution function along the i-th direction (i = 0, 1, 2, … 18), $\mathbf{r}$ is the position of the lattice, $\mathbf{e}_i$ is the local particle velocities, Δt is the time increment, and τ is the collision time. Moreover, the equilibrium distribution function $f_i^{\mathrm{eq}}(\mathbf{r}, t)$ is defined as

$$f_i^{\mathrm{eq}}(\mathbf{r},t)=w_i\rho(\mathbf{r})\left[1+3\frac{\mathbf{e}_i\cdot\mathbf{u}}{c^2}+\frac{9}{2}\frac{(\mathbf{e}_i\cdot\mathbf{u})^2}{c^4}-\frac{3}{2}\frac{\mathbf{u}^2}{c^2}\right], \tag{S2}$$

where the weight w_i are 1/3 for the rest particles (i = 0), 1/18 for i = 1 ~ 6 and 1/36 for i =7 ~ 18, respectively. c is the basic speed on the lattice. $\rho(\mathbf{r})$ and $\mathbf{u}$ respectively represent the fluid density and velocity and they are defined as follows

$$\rho=\sum_{i=0}^{18} f_i, \qquad \mathbf{u}=\frac{\sum_{i=0}^{18} f_i\mathbf{e}_i}{\rho}. \tag{S3}$$

By incorporating nonlocal interactions among the fluid particles, we can simulate the interfacial energy. Regarding the approach developed by Shan and Chen,[7] we consider a fluid-fluid interaction as follows

$$\mathbf{F}_{\mathrm{G}}(\mathbf{r})=-G\psi(\mathbf{r})\sum_{i=0}^{18} w_i\psi(\mathbf{r}+\mathbf{e}_i)\mathbf{e}_i, \tag{S4}$$

where the weight w_i are 0 for $|\mathbf{e}_i|$ = 0, 1/18 for $|\mathbf{e}_i|$ = 1 and 1/36 for $|\mathbf{e}_i|=\sqrt{2}$, respectively. G represents the interaction strength, and we adopt $\psi(\mathbf{r})$ = 1 – exp[– $\rho(\mathbf{r})$] as the interaction potential. Moreover, we use the following interaction potential as the interaction between the fluid and solid phases

$$\mathbf{F}_{\mathrm{w}}(\mathbf{r})=-G_{\mathrm{w}}\psi(\mathbf{r})\sum_{i=0}^{18} w_i s(\mathbf{r}+\mathbf{e}_i)\mathbf{e}_i, \tag{S5}$$

where G_{w} represents the interaction strength between the fluid and solid. s = 0 and s = 1 are defined for the corresponding lattice points where they are in fluid and solid phases, respectively. The fluid-fluid interfacial energy and solid-fluid interfacial energy are adjusted by changing the

fluid-fluid interaction strength G and the solid-fluid interaction strength G_w, respectively. By this way, we can simulate the contact angle ranging from 0° to 180°.

When we take consideration of the fluid-fluid interaction and the fluid-solid interaction, the local fluid velocity is determined as follows

$$\mathbf{u}'(\mathbf{r}) = \mathbf{u}(\mathbf{r}) + \frac{\tau}{\rho(\mathbf{r})}\left[\mathbf{F}_G(\mathbf{r}) + \mathbf{F}_w(\mathbf{r}) + \rho(\mathbf{r})\mathbf{g}\right], \tag{S6}$$

where $\mathbf{u}'(\mathbf{r})$ is the updated fluid velocity of the next iteration.

S2.2. Description of the simulation systems

LBM has its own unit, i.e., size (lu), mass (mu) and time (ts). Since we do not consider the size effect, we use dimensionless formulas in the LBM simulations. Moreover, different contact angles are realized by varying the value of G_w. The box size in our simulations is given as 160 lu × 160 lu × 40 lu (length × width × height), and the entire time step is typically on the order of 10^4 ts.

In experiments, the film is gradually added with DI water through a syringe pump and its volumes increases due to the supplement. To simulate the supplement of the water, in our simulations, we set a source which is always in the central axis, and 30 lu away from the edge of the box, and the source has a cuboid shape of 8 lu × 4 lu × 2 lu (length × width × height) which is very small compared with the film. To suppress the dynamics, the source with outflow of a very small mass flow rate is employed to guarantee that the droplet quasi-statically increases. We have to emphasize that in this study, we mainly focus on the quasi-static process, but not the dynamic process.

S3. Extracting the critical area

We adopt the procedure introduced by Lv *et al.*[8] to extract the critical area A_c from the experiment data. However, it should be noted that Lv *et al.* used the diameter of the hole *d*

whereas we use the area of the hole A. As a result, the equations derived by Lv *et al.* take on different forms in our study. The procedure is based on the assumption that the height of the liquid layer remains relatively constant. The height is estimated as $h = 2l_c\sin(\theta_s/2)$ [9].

The symbols used here to present time, hole area and liquid volume are t, A and Ω, respectively. The rate of volume change in the liquid layer corresponds to the flow rate of the liquid supply, i.e.,

$$Q = \frac{\mathrm{d}\Omega}{\mathrm{d}t} = -2l_c \sin\left(\frac{\theta}{2}\right)\frac{\mathrm{d}A}{\mathrm{d}t} \tag{S7}$$

where Q = 1ml min^{-1} represent the constant volumetric flow rate of the syringe pump. The second equality in equation (S7) is based on the assumption that any changes in the height of liquid layer is negligible. By integrating equation (S7) under the initial condition $A|_{t=0} = A_0$, where A_0 represents the initial hole area, we arrive at the following relation,

$$A(t) = A_0 - \frac{Q}{2l_c \sin\left(\frac{\theta}{2}\right)}t \tag{S8}$$

The procedure for determining the critical hole area A_c from the experimental data is described as follows. It should be noted that equation (S8) is expected to be applicable only when the hole area is sufficiently larger than the critical area. In each of the experimental curves shown in figure 5(*b*), we select the rightmost data point (corresponding to the largest value of $(t_0 - t)$) as A_0. This choice allows us to determine the specific form of (S8) for each considered value of d. we assume that the critical hole area is reached when the experimental curve deviates by a predetermined amount from the curve defined by (S8). In figure S3, we present the results of an experiment conducted in a container with d = 6.6 cm, which serves as a reference. The first experimental data point is chosen as A_0 in equation (S8). The numerical results obtained through SE suggest that the critical area in this case, taken as $A_c \approx 1.18$ cm^2, is presented as a red dot in figure S3. The deviation between the red dot and the corresponding value of our model, $A(t_c)$, can be characterized by defining a dimensionless ratio $\varepsilon = (A(t_c) - A_c)/A_c$, which takes a value of ≈ 6.72% for the specific case under consideration. Therefore, to determine the critical area

for other container sizes, we assume the same derivation of $\varepsilon = 6.72$ % between the experimental data and the model curve.

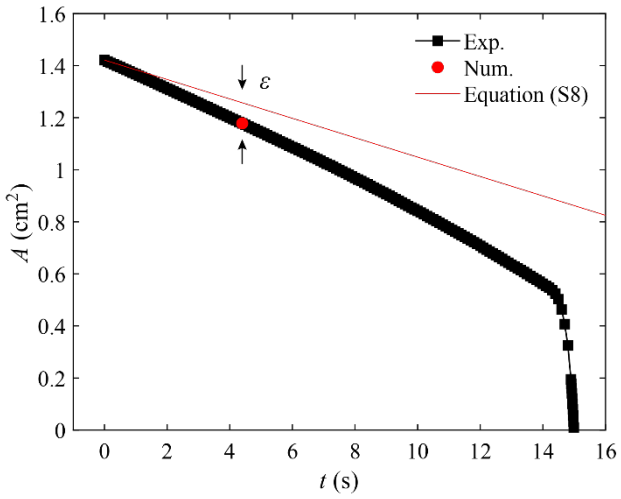

Fig S3. Procedure for computing the characteristic deviation ε. The black squares are the experimental data obtained in the smallest container ($d = 6.6$ cm, see figure 5(*b*)). The red dot in the diagram represents A_c as obtained from the SE results. The solid red line is the result of (S8).

S4. Comparison between the SE results and LBM results

We present a comparison between the SE results and LBM results as shown in figure S4. The black circles and red squares represent the SE results and LBM results, respectively. The diameter of the container is $d = 6$ cm, and the contact angles of the substrate and the wall are $\theta_s = 120°$ and $\theta_w = 90°$, respectively. The SE results and LBM results are consistent with each other.

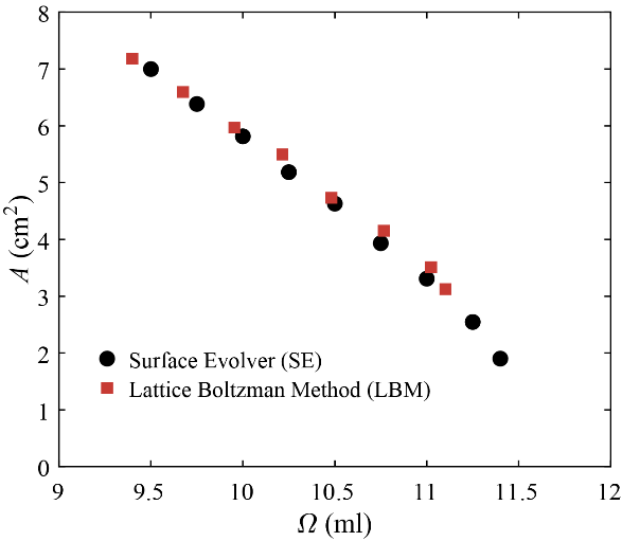

Fig S4. Dependency of the hole area A on the liquid volume Ω. The black circles and red squares represent the SE results and LBM results, respectively. The contact angles of the substrate and the wall are $\theta_s = 120°$ and $\theta_w = 90°$, respectively. The diameter of the container is $d = 6$ cm.

S5. Relationships of A vs. Ω and A vs. h

In order to get a comprehensive understanding of the relationships among A, h and Ω, we here provide a graph illustrating the dependence of Ω on A, as well as the dependence of h on A as shown in figure S5. The dense data points and the black hollow circles represent theoretical results and SE simulation results, respectively. In figure S5(a) and (b), the container diameter is fixed at $d = 9$ cm, and with contact angles $\theta_s = \theta_w$ ranging from 90°, 120°, 150° to 180°. In figure S5(c) and (d), the contact angles are fixed at $\theta_s = 160°$ and $\theta_w = 90°$, and circular containers with five different diameters d are employed, i.e., $d = 7$ cm, 9 cm, 11 cm, 13 cm, 15 cm. Ω_c and A_c respectively denote the critical values of the liquid volume and the hole area when instability occurs. The dashed lines in (b) and (d) denote $h = 2l_c\sin(\theta_s/2)$.

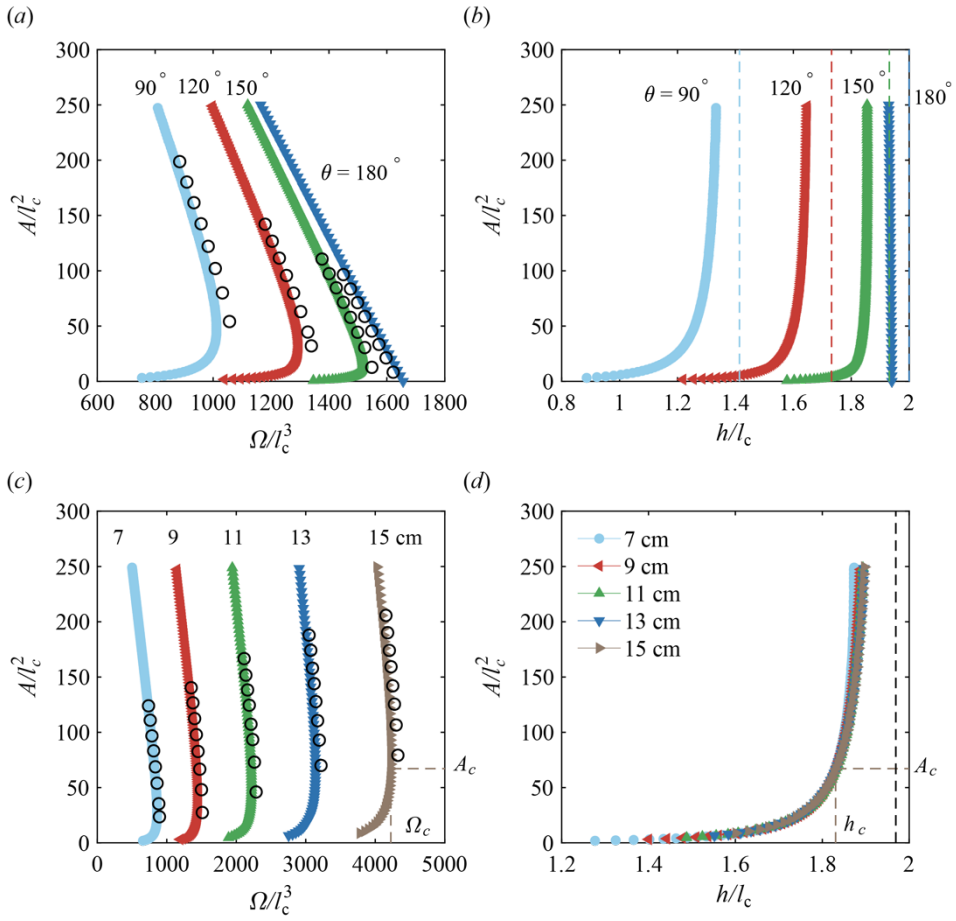

Fig S5. Numerical solutions illustrating the dependence of Ω on A, as well as the dependence of A on h, in dimensionless form. The dense data points represent theoretical results, while the black hollow circles represent the results obtained from SE simulations. (*a*) and (*b*): The container diameter is fixed at d = 9 cm, with contact angles $\theta_s = \theta_w$ ranging from 90°, 120°, 150° to 180° being considered. (*c*) and (*d*): The contact angles are fixed at θ_s = 160° and θ_w = 90°. Circular containers with five different diameters d are employed, i.e., d = 7 cm, 9 cm, 11 cm, 13 cm, 15 cm. Ω_c and A_c respectively denote the critical values of the liquid volume and the hole area when instability occurs. The dashed lines in (*b*) and (*d*) denote $h = 2l_c\sin(\theta_s/2)$.

S6. Alternative theoretical model

We here derived an alternative theoretical model, which can be verified to be equivalent to the model derived in §4.1 later. In this derivation, we employed the same assumptions and process as outlined in §4.1, with the corresponding geometry presented in figure S6.

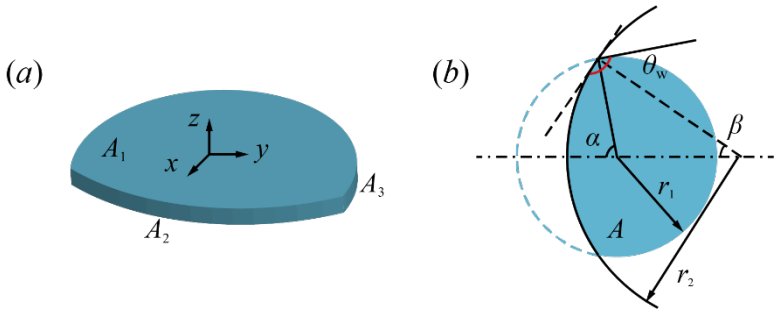

Figure S6. Simplified liquid layer profiles shown from (*a*) an oblique view and (*b*) a top view. Relevant geometric parameters are defined.

As depicted in figure S6, the relationship between θ_w, α and β can be expressed as $\theta_w + \alpha - \beta = \pi$. In addition, the areas of the characteristic surfaces, namely A_1, A_2 and A_3, can be calculated as follows: $A_1 = r_1^2(\pi - \alpha + \sin\alpha\cos\alpha) + r_2^2(\beta - \sin\beta\cos\beta)$, $A_2 = 2\beta r_2 h$ and $A_3 = 2r_1(\pi - \alpha)h$, where r_1 and r_2 satisfy the condition $r_1\sin\alpha = r_2\sin\beta$. The total free energy of the system, which includes the surface energy and gravity potential, can be written as $E = E_s + E_g = A_1\gamma(1 - \cos\theta_s) + A_2\gamma - A_3\gamma\cos\theta_w + \rho\Omega gh/2$.

For convenience, by employing the radius of the liquid layer r_1 as a reference, we introduce dimensionless forms of the relevant geometric and physical quantities as follows

$$\tilde{A}_1 = \frac{A_1}{r_1^2},\ \tilde{A}_2 = \frac{A_2}{r_1^2},\ \tilde{A}_3 = \frac{A_3}{r_1^2},\ \tilde{E} = \frac{E}{r_1^2\gamma},\ \tilde{h} = \frac{h}{r_1},\ \tilde{\Omega} = \frac{\Omega}{r_1^3}. \tag{S9}$$

Consequently, we rewrite A_1, A_2, A_3 and E into the following dimensionless forms

$$\tilde{A}_1 = \left(\pi - \alpha + \sin\alpha\cos\alpha\right) + \frac{\sin^2\alpha}{\sin^2\beta}\left(\beta - \sin\beta\cos\beta\right), \tag{S10}$$

$$\tilde{A}_2 = 2\frac{\sin\alpha}{\sin\beta}\beta\tilde{h}, \tag{S11}$$

$$\tilde{A}_3 = 2\left(\pi - \alpha\right)\tilde{h}, \tag{S12}$$

$$\tilde{E} = \tilde{A}_1\left(1 - \cos\theta_s\right) + \tilde{A}_2 - \tilde{A}_3\cos\theta_w + \frac{1}{2}\tilde{\Omega}\tilde{h}\left(\frac{r_1}{l_c}\right)^2. \tag{S13}$$

In order to determine the equilibrium profile of the liquid, we calculate the derivative of the energy in terms as α and set it equal to zero, i.e.,

$$\frac{\partial\tilde{E}}{\partial\alpha} = 0. \tag{S14}$$

In addition, considering the constraint

$$\tilde{\Omega} = \tilde{A}_1\tilde{h} = \text{constant}, \tag{S15}$$

we have $\partial\Omega/\partial\alpha = 0$, thus, the following relation can be obtained

$$\frac{\partial\tilde{h}}{\partial\alpha} = -\frac{\tilde{h}}{\tilde{A}_1}\cdot\frac{\partial\tilde{A}_1}{\partial\alpha}. \tag{S16}$$

Substituting equations (S10) - (S13) and (S16) into equation (S14), we obtain the dimensionless value of the liquid layer thickness as follows

$$\tilde{h} = \frac{\partial\tilde{A}_1}{\partial\alpha}\left(1 - \cos\theta_s\right)\cdot\left\{\left[2\beta\frac{\sin\alpha}{\sin\beta} - 2\left(\pi - \alpha\right)\cos\theta_w + \frac{1}{2}\tilde{\Omega}\left(\frac{r_1}{l_c}\right)^2\right]\frac{1}{\tilde{A}_1}\frac{\partial\tilde{A}_1}{\partial\alpha}\right.$$
$$\left. -2\frac{\sin\alpha}{\sin\beta} + \frac{2\beta}{\sin^2\beta}\left(\sin\alpha\cos\beta - \cos\alpha\sin\beta\right) - 2\cos\theta_w\right\}^{-1}, \tag{S17}$$

where

$$\frac{\partial \tilde{A}_1}{\partial \alpha} = 2\frac{\sin^2\alpha}{\sin^2\beta} + 2\beta\left(\frac{\sin\alpha\cos\alpha}{\sin^2\beta} - \frac{\sin^2\alpha\cos\beta}{\sin^3\beta}\right) - 2\frac{\sin\alpha\cos\alpha\cos\beta}{\sin\beta} + \cos^2\alpha - \sin^2\alpha - 1 . \quad \text{(S18)}$$

The solution of equation (S17) is obtained and is presented in figure S7. It is evident from figure S7 that the results derived from the model presented here are the same as those obtained in the manuscript (see §4.1). In other words, the two approaches for derivation are equivalent.

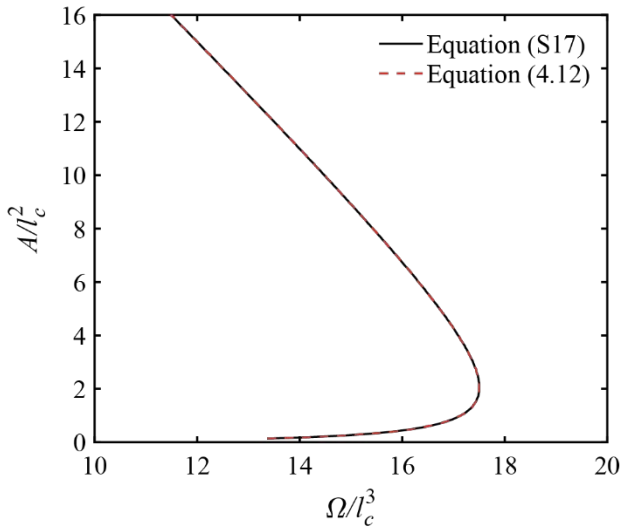

Figure S7. Solutions of equation (S17) and equation (4.12) illustrating the dimensionless relationship between Ω on A. The black solid line and the red line represent the solutions of equation (S17) and equation (4.12), respectively. The diameter of the container is d = 7 cm, and the contact angles are θ_s = 160° and θ_w = 90°.

S7. Theoretical model with correcting coefficients

We derived the model in §4 neglecting the meridional curvature which results in the miss of an energy penalty for having the liquid-vapor surface area A_1 and A_2. To fix this problem, we here introduced the two coefficients c_1 and c_2 for the two parts of the liquid-vapor surface A_1 and A_2 in our model, respectively, to modify the effective liquid-vapor interfacial energy. Therefore, the surface energy of the system is rewritten as $E_s = A_1\gamma(c_1 - \cos\theta_s) + c_2A_2\gamma - A_3\gamma\cos\theta_w$, where c_1 and c_2 are the correcting coefficients for the liquid-vapor surface A_1 and A_2. Following the

same steps as described in §4.1, we can finally obtain

$$\tilde{h}=\frac{\partial\tilde{A}_1}{\partial\alpha}\left(c_1-\cos\theta_s\right)\cdot\left\{\left[2c_2\beta\frac{\sin\alpha}{\sin\beta}-2\left(\pi-\alpha\right)\cos\theta_w+\frac{1}{2}\tilde{\Omega}\left(\frac{r_1}{l_c}\right)^2\right]\frac{1}{\tilde{A}_1}\frac{\partial\tilde{A}_1}{\partial\alpha}\right.$$
$$\left.+2\frac{c_2\sin\alpha}{\sin\beta}-\frac{2c_2\beta}{\sin^2\beta}\left(\sin\alpha\cos\beta+\cos\alpha\sin\beta\right)-2\cos\theta_w\right\}^{-1} \tag{S19}$$

We determine the coefficients c_1 and c_2 in the following manner. As an example, we select a container with a diameter of d = 6.6 cm and contact angles of $\theta_s = \theta_w$ = 110°. The volume of the liquid film is set at Ω = 12.0 ml, serving as a reference. Once the liquid layer with a stable hole at the wall is formed, the liquid-vapor area consists of two parts, the upper liquid-vapor area A_1 and the side liquid-vapor area A_2. Subsequently, we extracted the two surface areas A_1 and A_2 separately from the SE simulation and the theoretical model. From the SE simulation, we find that the upper liquid-vapor surface area is A_1^{SE} = 28.476 cm^2, while in the theoretical model, it is A_1^{model} = 29.236 cm^2. Hence, we define c_1 as $c_1 = A_1^{SE}/A_1^{model}$ = 28.476/29.236 = 0.97. Similarly, for the side liquid-vapor surface area, we find A_2^{SE} = 1.332 cm^2 in the SE simulation and A_2^{model} = 2.016 cm^2 in the theoretical model. Consequently, we define c_2 as $c_2 = A_2^{SE}/ A_2^{model}$ =1.332/2.016 = 0.66. After that, by substituting the correcting coefficients c_1 = 0.97 and c_2 = 0.66 into equation (S19), we finally obtain the dimensionless relationship between A and Ω, as illustrated in figure S8. We can see from figure S8 that the model with correcting coefficients is consistent with SE simulations.

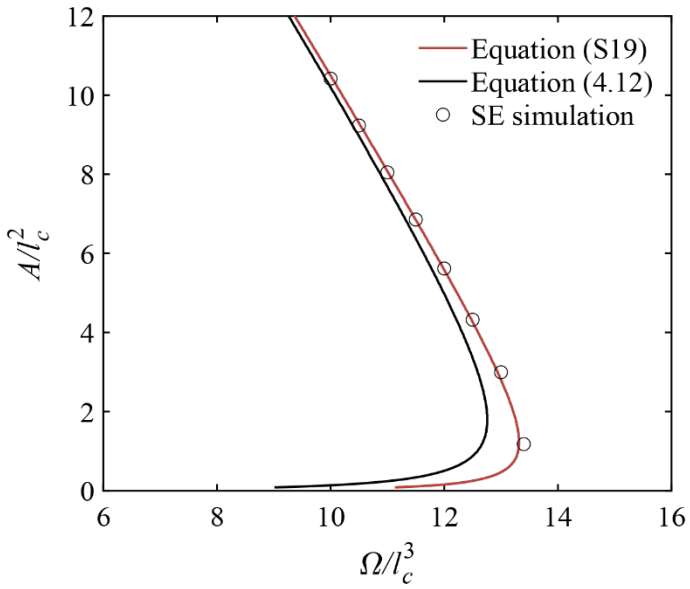

Figure S8. Comparison of Ω on A in dimensionless form between different methods. The black line represents the solution of the model (i.e., equation (4.12) in the main text) without the correcting coefficients. The red line represents the solution of the model (i.e., equation (S19)) with the correcting coefficients, where c_1 = 0.97 and c_2 = 0.66. The black hollow circles represent the results of the Surface Evolver simulation. The diameter of the container is d = 6.6 cm, and the contact angle is $\theta_s = \theta_w$ = 110°.

It is important to note that the liquid-vapor surface area is 29.808 cm^2 and 31.252 cm^2 in SE simulation and theoretical model, respectively, and the difference between the two is only (31.252 – 29.808)/29.808 ≈ 4.54%, which indicates our assumption of a flat liquid film in the manuscript is reasonable. Even though the corrected model exhibits more excellent consistency with SE simulation, the discrepancy in surface area between the two model is minimal. Furthermore, the model presented in the manuscript is able to effectively capture the underlying physical mechanism.

S8. Analysis of the scaling exponent in the dynamic behavior of hole collapse

The scaling exponent in the dynamic behavior of hole collapse is sensitive to the choice of t_0. Strictly speaking, t_0 is defined as the moment when $A = 0$. However, accurately determining the value of t_0 from experiments is very difficult due to the limited frame rate of the high-speed camera. In other words, close to the singularity t_0, for a single recording, the first frame chosen must have either $t > t_0$ or $t < t_0$ with $|t - t_0| < \delta t$. δt represents the time interval between two

neighboring frames (i.e., the first and the second frames), e.g., $\delta t = 5\times10^{-5}$ s when the frame rate is 20 000 fps.

For a single trial in the practical experiment, t_0 is determined as the moment captured in the snapshot just prior to the closure of the hole. Once t_0 is determined, we can obtain the corresponding hole area A for a given value of $(t_0 - t)$. Subsequently, the same experiment is conducted five times to generate five data sets reflecting the relationship between A and $(t_0 - t)$. After that, for each time point $(t_0 - t)$, we calculate the average value of the hole area A based on these five experiments. Finally, we present $(t_0 - t)$ and the corresponding average value of A as figure17. In this case, since t_0 is approximately determined, we denoted it as $t_0 \approx t_0^{\text{approx}}$.

To ensure a comprehensive understanding, we choose t_0 using three different approaches: (1) $t_0 \approx t_0^{\text{approx}}$ (as stated in the above); (2) $t_0 \approx t_{-1} = t_0 - \delta t$; (3) $t_0 \approx t_{+1} = t_0 + \delta t$. In addition, we tried to fit the experimental data using an exponent of 1. Figure S9 illustrates the dependence of A on $(t_0 - t)$ using these three approaches to determined t_0. It is evident that an exponent of 1.1 provides the best fit for our experimental data.

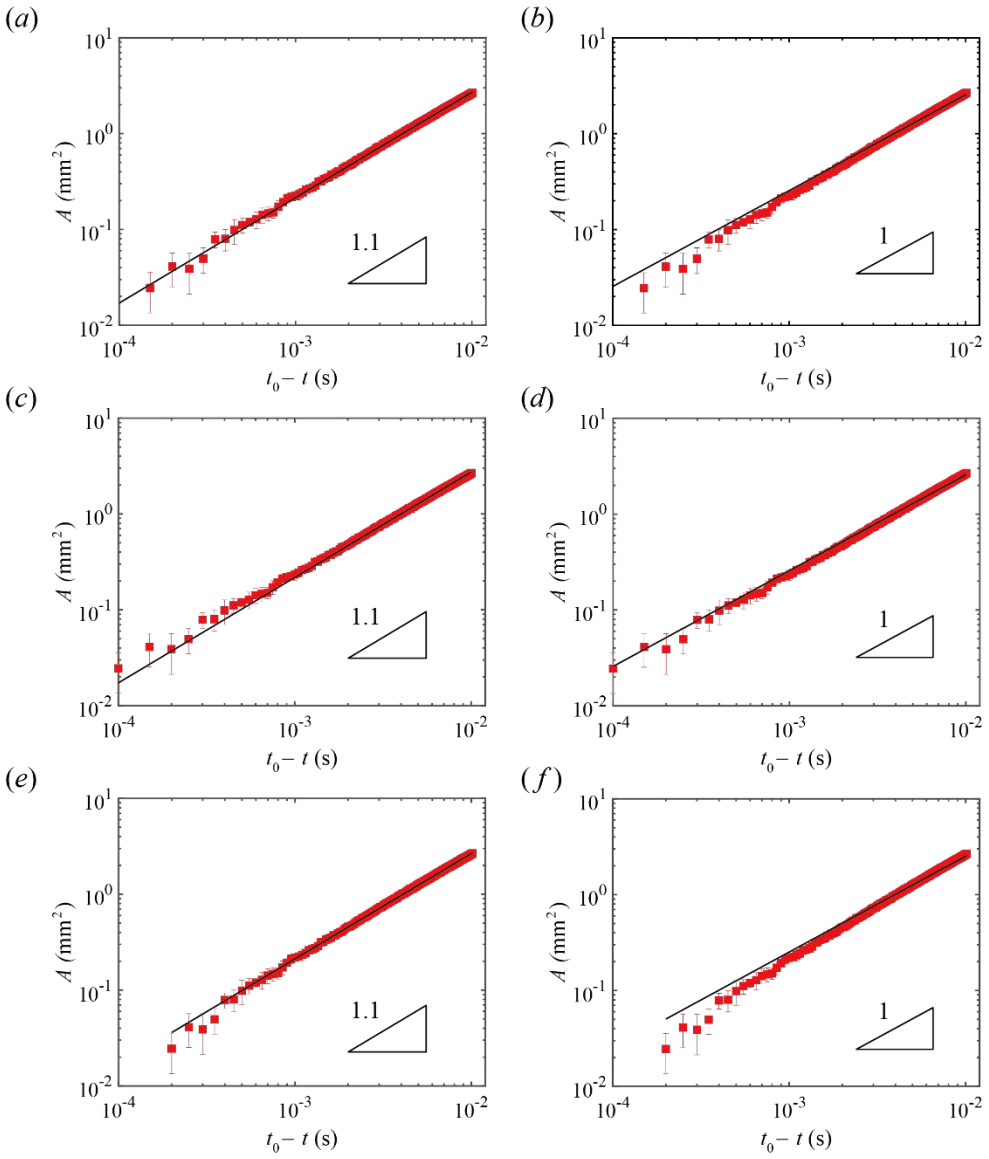

Figure S9. Time evolution of the hole area A in wetting mode II. Here, t denotes the time and t_0 is defined as the moment when the hole is completely closed. The red squares are experimental data with error bars, and the black solid line is the fit to the experimental data based on the scaling law of $A \sim (t_0 - t)^{1.1}$ (*a*, *c* and *e*) or $A \sim (t_0 - t)^1$ (*b*, *d* and *f*). The data in (*a*) and (*b*) is from figure 17 in the main text, i.e., $t_0 \approx t_0^{\text{approx}}$. In (*c*) and (*d*), we choose $t_0 \approx t_{-1} = t_0 - \delta t$. In (*e*) and (*f*), we choose the $t_0 \approx t_{+1} = t_0 + \delta t$.

S9. Supplementary Movies

Video S1. Wetting mode I of the film observed in the experiment. The movie shows the entire processes of the wetting mode I of the film. The geometrical parameters of the container is d = 9 cm, and the flow rate is Q = 1 ml/min. The substrate and wall are both coated with

Glaco. When the film is added with DI water, it gradually wets the container. As time processes, the film gradually fills the container and finally evolves to a uniform film at t = 161.3 s.

Video S2. Wetting mode II of the film observed in the experiment. The movie shows the entire processes of the wetting mode II of the film. The geometrical parameters of the container is d = 9 cm, and the flow rate is Q = 0.1 ml/min. The substrate is coated Glaco, and the wall is treated with commercial hydrophobic coating.

Video S3. Wetting mode III of the film observed in the experiment. The movie shows the entire processes of the wetting mode III of the film. The geometrical parameters of the container is d = 9 cm, and the flow rate is Q = 0.1 ml/min. The substrate is coated Glaco, and the wall is not treated with coatings.

Video S4. Wetting mode I of the film obtained by employing LBM simulations. The movie shows the entire processes of the wetting mode I of the film obtained by employing LBM simulation. The diameter of the container is d = 160 lu, and the contact angles of the substrate and the wall are 120° and 180°, respectively.

Video S5. Wetting mode II of the film obtained by employing LBM simulations. The movie shows the entire processes of the wetting mode I of the film obtained by employing LBM simulation. The diameter of the container is d = 160 lu, and the contact angles of the substrate and the wall are 120° and 90°, respectively.

Video S6. Wetting mode III of the film obtained by employing LBM simulations. The movie shows the entire processes of the wetting mode I of the film obtained by employing LBM simulations. The diameter of the container is d = 160 *lu*, and the contact angles of the substrate and the wall are 120° and 35°, respectively.

Video S7. The final stage of the hole collapse in wetting mode II. The movie shows the final

stage of the hole collapse in wetting mode II. The geometrical parameters of the container is d = 9 cm. The substrate is coated Glaco, and the wall is treated with commercial hydrophobic coating.

S10. Supplementary references

[1] S. Chen, G. D. Doolen, Lattice Boltzmann method for fluid flows, *Annu. Rev. Fluid Mech.* **1998**, *30*, 329.

[2] N. S. Martys, H. Chen, Simulation of multicomponent fluids in complex three-dimensional geometries by the lattice Boltzmann method, *Phys. Rev. E* **1996**, *53*, 743.

[3] A. S. Joshi, Y. Sun, Multiphase lattice Boltzmann method for particle suspensions, *Phys. Rev. E* **2009**, *79*, 066703.

[4] Y. Yu, Y. Liu, Lattice-Boltzmann models simulation of wetting modes on the surface with nanostructures, *J. Comput. Theor. Nanos.* **2008**, *5*, 1377.

[5] K. A. Raman, R. K. Jaiman, T.-S. Lee, H.-T. Low, Lattice Boltzmann simulations of droplet impact onto surfaces with varying wettabilities, *Int. J. Heat Mass Transfer* **2016**, *95*, 336.

[6] Illner, R. *Lattice Boltzmann Modeling: An Introduction for Geoscientists and Engineers*. JSTOR, 2007.

[7] X. Shan, H. Chen, Lattice Boltzmann model for simulating flows with multiple phases and components, *Phys. Rev. E* **1993**, *47*, 1815.

[8] C. Lv, M. Eigenbrod, S. Hardt, Stability and collapse of holes in liquid layers. *J. Fluid Mech.* **2018**, *855*, 1130–1155.

[9] P.-G. De Gennes, F. Brochard-wyart, D. Quéré, *Capillarity and Wetting Phenomena*. Springer, 2003.